Experimental demonstration of a three-dimensional bioinspired tonotopic metasensor

INTERFACE

royalsocietypublishing.org/journal/rsif

Research

Cite this article: Liu Y, Zhang H, Riva E, Pugno NM, Gliozzi AS, Bosia F, Tortello M. 2026 Experimental demonstration of a three-dimensional bioinspired tonotopic metasensor. *J. R. Soc. Interface* **23**: 20250771. https://doi.org/10.1098/rsif.2025.0771

Received: 25 July 2025
Accepted: 25 November 2025

Subject Category:
Life Sciences–Physics interface

Subject Areas:
biomechanics, biophysics

Keywords:
bioinspired materials, metamaterials, cochlea, elastic waves

Author for correspondence:
Mauro Tortello
e-mail: mauro.tortello@polito.it

Electronic supplementary material is available online at https://doi.org/10.6084/m9.figshare.c.8230394.

THE ROYAL SOCIETY PUBLISHING

Experimental demonstration of a three-dimensional bioinspired tonotopic metasensor

Yuxuan Liu[1], Han Zhang[1], Emanuele Riva[2], Nicola M. Pugno[3,4], Antonio S. Gliozzi[1], Federico Bosia[1] and Mauro Tortello[1]

[1]Dipartimento di Scienza Applicata e Tecnologia, Politecnico di Torino, Torino, Italy
[2]Dipartimento di Meccanica, Politecnico di Milano, Milano, Italy
[3]Mechano-X Labs, Dipartimento di Ingegneria Civile, Ambientale e Meccanica, Università di Trento, Trento, Italy
[4]School of Engineering and Materials Science, Queen Mary University of London, London, UK

ER, 0000-0001-6773-9000; NMP, 0000-0003-2136-2396; ASG, 0000-0003-1084-0444; FB, 0000-0002-2886-4519; MT, 0000-0002-9953-9000

Spiral structures are widely recurrent in nature to serve different purposes, including the spatial mapping of acoustic frequencies in the mammalian cochlea—a feature referred to as tonotopy. Motivated by this fundamental characteristic, we explore the elastodynamics of a three-dimensional seashell-like structure with frequency-selective capabilities and, in addition, a polarization-dependent response, a feature rarely found in nature. We experimentally demonstrate how these properties can be exploited to discriminate between out-of-plane and in-plane waves, while producing a discrete spectrum that displays tonotopic behaviour. The polarization capabilities are a consequence of the realization of a tonotopic response in the spiral plane and perpendicular to it. Results can be of interest for the design of low-power, low-latency smart sensors for structural health monitoring and non-destructive testing, where discrimination between frequency and polarization is usually accomplished through digital signal processing.

1. Introduction

Nature has been a longstanding source of inspiration for the development of advanced materials and devices due to its highly optimized structural and functional designs. In recent years, it has become apparent that biological architectures can also inspire the design of optimized structures for wave and vibration control, since many such examples occur in natural systems [1]. In particular, spiral geometries are pervasive in biological systems, where they often serve multifunctional roles in mechanical adaptability, energy storage and signal transduction.

The most well-known example is the cochlea of the mammalian inner ear, which performs frequency decomposition for sound processing through its graded 'tonotopic' spiral structure [2–4]. The spiral shape of the cochlea allows a compact organization of a long basilar membrane within a small space. This facilitates tonotopic mapping, where different frequencies of sound waves stimulate different regions along its length, enhancing mechanical separation of sound frequencies and supporting efficient fluid wave propagation for auditory transduction [5]. Similarly, some insect species (e.g. moths, crickets) have curved tympanal membranes or associated tracheal structures that enhance frequency tuning and sound sensitivity [6,7]. The curved design helps in wave propagation and resonance tuning, allowing insects to detect predator sounds (like bats) with greater precision [8]. Another notable example of spiral structure is the chameleon's tongue apparatus, which stores elastic potential energy in coiled tissues for rapid projection. The chameleon's tongue

extension involves a coiled accelerator muscle and elastic collagen sheaths, and the coiled geometry allows for storing elastic potential energy efficiently, releasing it rapidly for high-speed movement: essentially a biomechanical spring [9]. The seahorse tail is another interesting example of spiral structure optimized for mechanical functionality, in this case prehensile and protective. The tail has a square cross-section with spirally arranged bony plates, enabling both flexibility and crush resistance. The spiral configuration allows the tail to twist and grip with precision while absorbing mechanical stress [10]. Other biological systems, such as gastropod and mollusc shells (e.g. the Turritellidae seashell), or ammonites, are characterized by their helical geometry and graded structure and display exceptional mechanical strength and vibrational damping properties [11,12].

Inspired by these natural designs, spiral elastic metamaterials have emerged as a promising class of engineered structures capable of manipulating mechanical inputs functionally. For instance, they allow mode conversion from longitudinal to twist [13], where their inherent geometric chirality and nonlinearity enable wave control, filtering and localization—properties that are particularly advantageous for advanced sensing applications [14–16]. In this context, space-coiling designs utilize spiral geometries to modulate sound waves through phase and amplitude control [17]. This family of metamaterials enables simultaneous tuning of multiple wave parameters, making them effective for applications including sound filtering and wavefront shaping [18]. Chiral metamaterials, characterized by their asymmetrical structures, interact uniquely with acoustic waves, inducing phenomena such as acoustic rotation and enhanced transmission [19]. By precisely tuning chiral properties, these materials can be designed to direct sound propagation, with promising applications in acoustic imaging, sensing and wave steering. Recent studies have demonstrated that cochlea-inspired chiral architectures can be engineered to exhibit negative refractive indices, enabling the development of novel acoustic lenses and cloaking devices [20,21]. In other studies, cochlea-bioinspired metamaterials have been demonstrated for rainbow trapping [22] and tonotopic sensing [23,24]. These two features share the property of concentrating elastic energy at different spatial locations corresponding to different frequencies [25–27]. However, in the case of a rainbow trapping structure (sometimes referred to as the 'metawedge' [28]), energy localization occurs at the site of individual resonators along the metamaterial, while in a continuous graded structure such as the cochlea-inspired one we are considering here, it is the modal shape that is responsible for frequency-dependent energy localization.

Recently, we have studied the vibration-control properties of seashell structures [29] and numerically investigated their tonotopic properties, as well as the possibility of discriminating between different polarization directions in the transmitted vibrations, in view of exploiting the concept for advanced sensing applications [30]. Metasensors with tonotopic properties can provide passive *in materia* frequency filtering of transmitted signals, while incorporating polarization sensitivity into sensor designs offers enhanced directional detection, providing a multidimensional approach to acoustic sensing and processing.

In this context, here we present an experimental realization of a bioinspired tonotopic metasensor that integrates a spiral elastic metamaterial architecture to achieve enhanced sensitivity and frequency selectivity along two different vibration directions, together with polarization-sensitive behaviour, offering a compact and scalable platform for detecting mechanical stimuli across a broad spectral range.

2. Methods

2.1. Parametric description of the surface

The geometry of seashell-inspired structures can be described by a set of parametric equations [11,30,31]. Therefore, let us now consider a seashell-inspired structure, with a circular cross-section and no axial pitch, i.e. planospiral. The central line, around which the cross-section can change radius $r(\theta)$ as a function of the curvilinear angle θ, thus describing the surface at different angles, can be represented by the following parametric equations in Cartesian coordinates:

$$\begin{cases} x = R_0 \cos\theta \exp\left(k_R \dfrac{\theta}{\theta_{max}}\right), \\ y = R_0 \sin\theta \exp\left(k_R \dfrac{\theta}{\theta_{max}}\right), \\ z = 0, \end{cases} \tag{2.1}$$

where R_0 is the initial curvature radius and k_R is the corresponding reduction factor, so that $R(\theta) = R_0 \exp\left(k_R \dfrac{\theta}{\theta_{max}}\right)$. $\theta_{max} = 2\pi \cdot n_T$, where n_T is the number of turns. If the cross-section is, in the simplest case, circular, it can be written as $r(\theta) = r_g \exp\left(k_b \dfrac{\theta}{\theta_{max}}\right)$, where r_g is the initial radius of the cross-section. $r(\theta)$ decreases as well with increasing angle θ depending on its corresponding reduction factor k_b. The thickness of the cross-section is taken as $\frac{r_g}{k_{th}}$, where k_{th} is a constant, in this case chosen equal to 15. Figure 1a–e reports several structures generated by using the above-given equations and by changing only the two reduction factors k_R and k_b. Nevertheless, significantly different geometries can be obtained. As discussed in more detail in [30], this kind of structure can be optimized to feature a tonotopic behaviour along two different vibration directions, namely in the plane of the spiral and perpendicular to it. The optimized structure is the one shown in figure 1e and its spectral properties are reported in figure 1f: coloured symbols indicate the normalized displacement as a function of the normalized curvilinear coordinate $\bar{\theta} = \theta/\theta_{max}$ and normalized logarithmic frequency $\bar{\omega} = \dfrac{\ln\left(\frac{\omega_i}{\omega_{min}}\right)}{\ln\left(\frac{\omega_{max}}{\omega_{min}}\right)}$, where ω_i is the eigenfrequency of the ith mode, $\omega_{min} = 100$ Hz and $\omega_{max} = 10$ kHz.

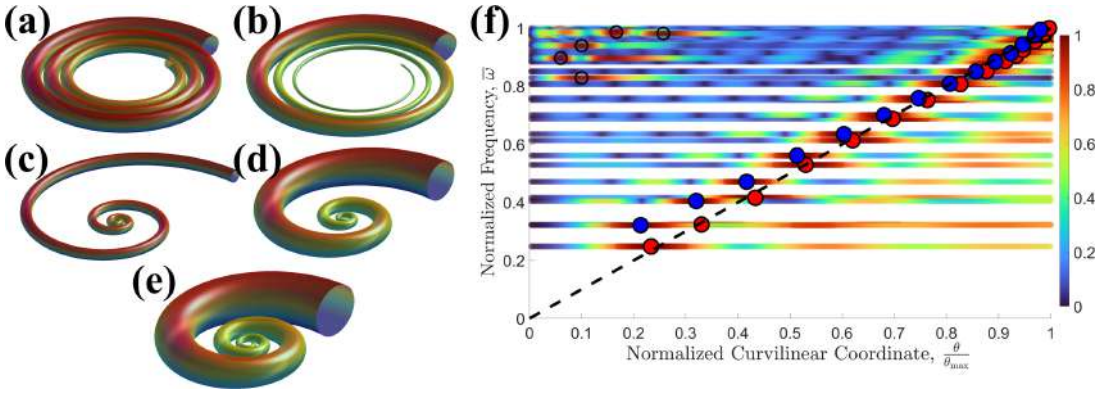

Figure 1. (a–e) Seashell-inspired planospiral structures generated by using the same set of parametric equations but with different parameters. (e) Structure optimized for the simultaneous in-plane and out-of-plane tonotopic behaviour, reported in panel (f).

Table 1. Geometrical parameters used for the fabrication of the device.

parameter	value	description
R_0	8.25 cm	initial curvature
k_R	−3.044	curvature reduction factor
θ_{max}	6π	maximum curvilinear angle
r_g	2.09 cm	initial cross-section radius
k_b	−2.609	cross-section reduction factor

For every curvilinear angle, the displacement has been averaged over 10 points along the cross-section and normalized to the maximum average obtained for all curvilinear angles at that eigenfrequency. Symbols indicate the maximum displacement for every eigenmode, and three different types of modes can be distinguished. In the top-left part of the plot, we can find the circumferential modes, represented by empty circles. Blue symbols represent modes that are vibrating mainly in the plane of the central line, which we will call XY modes, while red symbols indicate modes that predominantly oscillate perpendicularly to the plane containing the central line and that we will indicate as Z modes. The black dashed line is an ideal $\bar{\omega} = \bar{\theta}$ tonotopic line. It is possible to see that in the optimized structure, both XY and Z modes follow this line quite well, thus featuring this effect along two different perpendicular directions. Figure 1f reports the trend for the structure shown in figure 1e in the case of clamped-free boundary conditions.

With the aim of experimentally validating this kind of bioinspired metasensors, we fabricated one representative device, namely the optimized one reported in figure 1e, and experimentally characterized it.

2.2. Materials and device fabrication

The optimized metasensor was fabricated using 'Vero Black Plus' (Stratasys), a high-performance photopolymer resin specifically chosen for its excellent mechanical properties and suitability for vibration-based sensing applications. The material has a Young's modulus of 2–3 GPa, a density of 1170–1180 kg m^{-3} and a Poisson's ratio approximately equal to 0.33 [32,33]. The metasensor was manufactured using stereolithography three-dimensional (3D) printing technology. The printer used was the Stratasys J750^{TM}, six-material capacity, 14 µm resolution, accuracy up to 200 µm for full model size and the printing parameters were: high-mix/high-speed mode with a layer resolution thickness of 27 µm. The support material was SUP706B, which can be dissolved in a suitable solution of sodium hydroxide and sodium metasilicate. The slight anisotropy between the in-plane (build layer) and out-of-plane direction implies a negligible variation (less than 1%) of eigenfrequency values compared with an isotropic model. No visible defects, inhomogeneities or heterogeneities were observed in the printed samples. Overall, the quality of the 3D printing system guarantees a high level of predictability and reproducibility in the desired mechanical and acoustic performance. During the fabrication process, whenever overhanging parts or cavities need to be realized, the softer support material is deposited at the same time as the rigid photopolymer to prevent the collapse of the structure. In our case, the printed device was scaled up three times to allow better removal of such material. As a consequence, the spanned frequency range is reduced with respect to the device simulated originally. In general, it is well-known that the natural frequencies of structures like beams, rods, cylinders, cylindrical shells, etc., scale inversely with their dimensions [34]. In our case, R_0, r_g and thickness increase by a factor of $s = 3$. The scaling of the resonance frequency with the device size has also been verified by finite element method (FEM) simulations: if the geometry is scaled up by a factor s, the eigenfrequencies scale down exactly as $1/s$. Therefore, the frequency range where the tonotopy is expected to occur in the fabricated device is no longer 100 Hz ÷ 10 kHz, but is reduced to approximately 30 Hz ÷ 3.3 kHz. Table 1 reports the parameters necessary to generate the geometry, i.e. those for the central line in equation (2.1) and for the circular cross-section, $r(\theta)$.

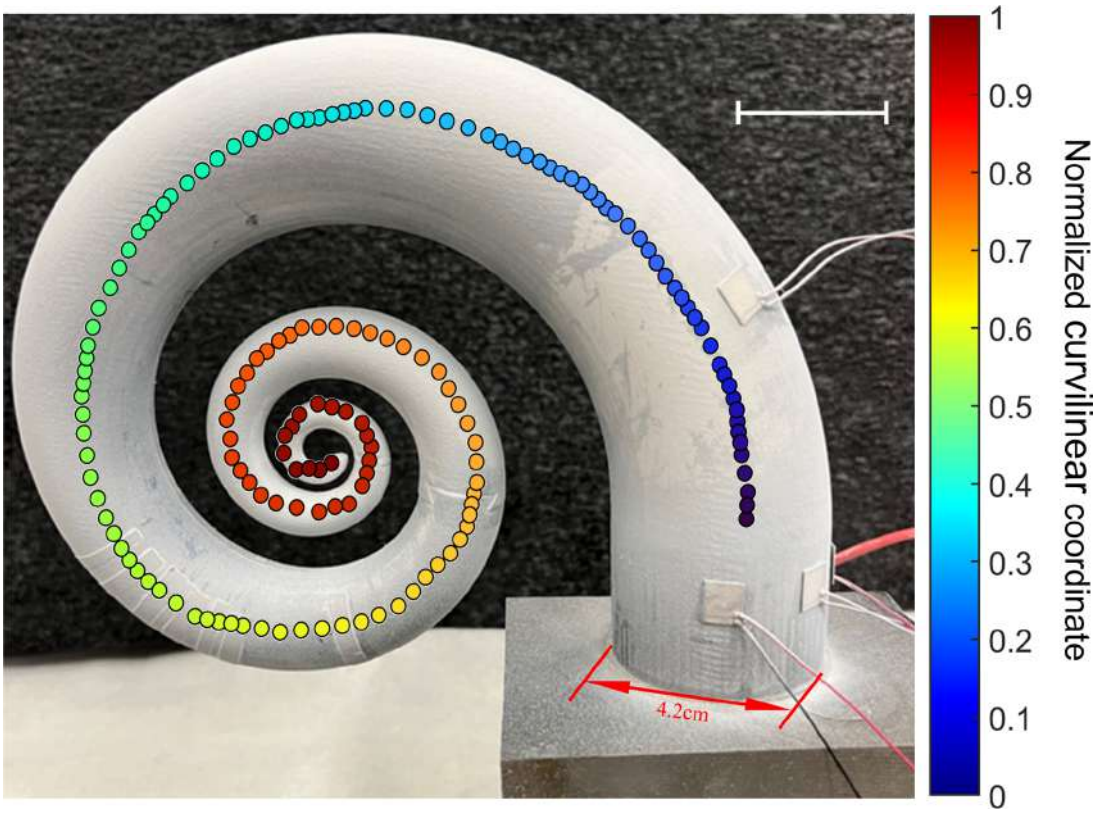

Figure 2. Experimental set-up for the three-dimensional LDV measurements. The boundary conditions are clamped-free, the coloured symbols represent the measurement points and the colour bar, from dark blue to dark red, corresponds to the normalized curvilinear angle $\overline{\theta} = \frac{\theta}{\theta_{max}}$, where θ is the curvilinear angle and $\theta_{max} = 6\pi$. The white scale bar corresponds to 3 cm, and the diameter of the initial cross-section is shown in red.

The frequency range used for the theoretical design of the device (100 Hz ÷ 10 kHz) was chosen so as to be in the audible range, given the reference to the mammalian cochlea and to possible applications as artificial cochlea devices. The scaling is due to mere limitations in the fabrication process of the printers available in our laboratory. Thus, while on the one hand, it is technologically possible to print a smaller device with more advanced printing techniques, on the other hand, in this work, we first of all aim at experimentally proving the concept. More generally, depending on the applications and the printing capabilities, the device can be scaled up or down. Finally, another possibility to tune the desired frequency range could also be to change the material.

2.3. Experimental set-up and testing procedure

A Polytec 3D Scanning Laser Doppler Vibrometer (LDV) system equipped with three PSV-500 scanning heads was used for vibration measurements. The system provides non-contact, high-resolution, high-frequency vibration measurements from DC to 25 MHz and, most importantly, it decouples the response velocity into three mutually perpendicular velocity components. This allows us to determine the vibration mode of the sample from the component–amplitude relationship of the response velocity. Figure 2 shows a picture of the device along with some of the piezo-transducers used to generate the vibrations. The end with the larger cross-section was glued to a heavy metallic cube to reproduce the clamped-free boundary conditions. The measured locations are represented by coloured symbols, and the colour scale is proportional to the normalized curvilinear coordinate. The measurements were performed on the 3D-printed sample by adopting two different types of boundary conditions, free–free and clamped-free. The excitation signal was applied by using a transducer designed to induce two pairs of counteracting bending moments at the surface of the sample. Three transducers were applied at three different positions to reproduce the 0°, 45° and 90° excitation directions, where the angle is considered with respect to the xy plane. This is important to study, as a function of the input signal direction, the spectral behaviour, especially in terms of activated modes and directional response (polarization). In the lower part of figure 2, we can see, in the front, the transducer used for the 90° excitation and, on its right, the 45° one. The 0° transducer is not visible, while the other one that can be seen mounted above was only used for the initial test of the set-up. For a more detailed view, it is also possible to see the insets in figure 3. The sample was excited with a chirp signal in the 50–3000 Hz frequency range.

2.4. Data processing and analysis

Tonotopy was evaluated by measuring, in the whole frequency range, the particle velocity response at various points along the curvilinear coordinate, all positioned on the surface of the device corresponding to the 90° direction, as already shown in figure 2.

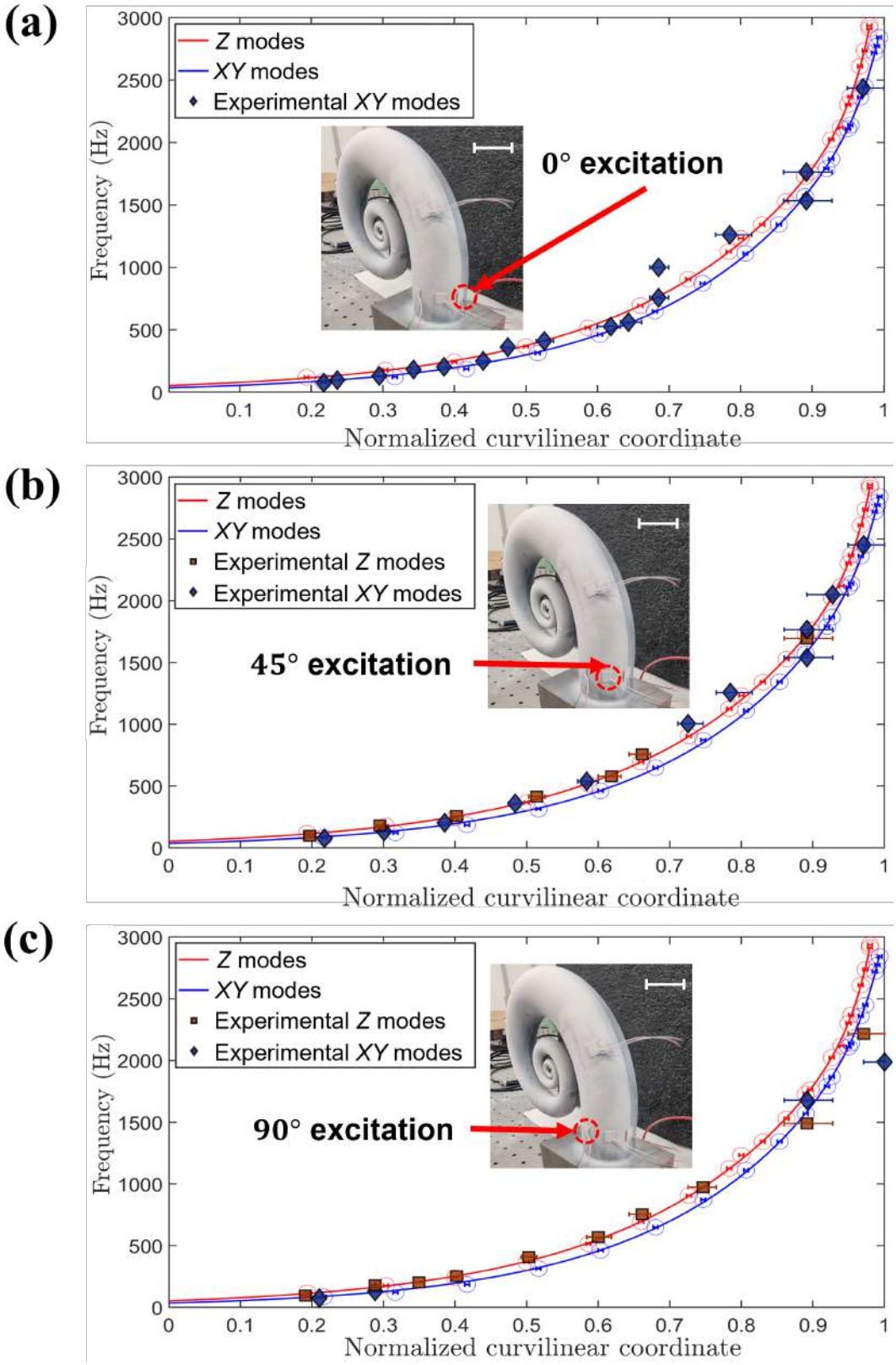

Figure 3. Tonotopic behaviour of the device under different excitation directions in the case of fixed-free boundary conditions. (a) 0°; (b) 45°; (c) 90°. Blue and red solid lines represent the tonotopic reference obtained by finite-element simulation, while the circular symbols indicate the frequency versus maximal response location of the simulated eigenmodes. Diamonds and squares represent the frequency versus normalized curvilinear angle for the experimental *XY* and *Z* modes, respectively. Error bars are obtained by taking into account the fact that the displacements are calculated or measured on a limited number of locations. The white scale bar in the insets corresponds to 3 cm.

This is the most convenient choice that allows access to all the curvilinear angle range. As expected, for each of the three velocity components, u, v and w, the response spectra exhibit amplitude peaks at the resonance frequencies of the device (figure 4).

For each location, the response velocity spectrum was analysed by considering the xy component (the square root of the sum of the squared x and squared y components, $\sqrt{u^2 + v^2}$), and the z component (the absolute value of the z component, $|w|$), thus

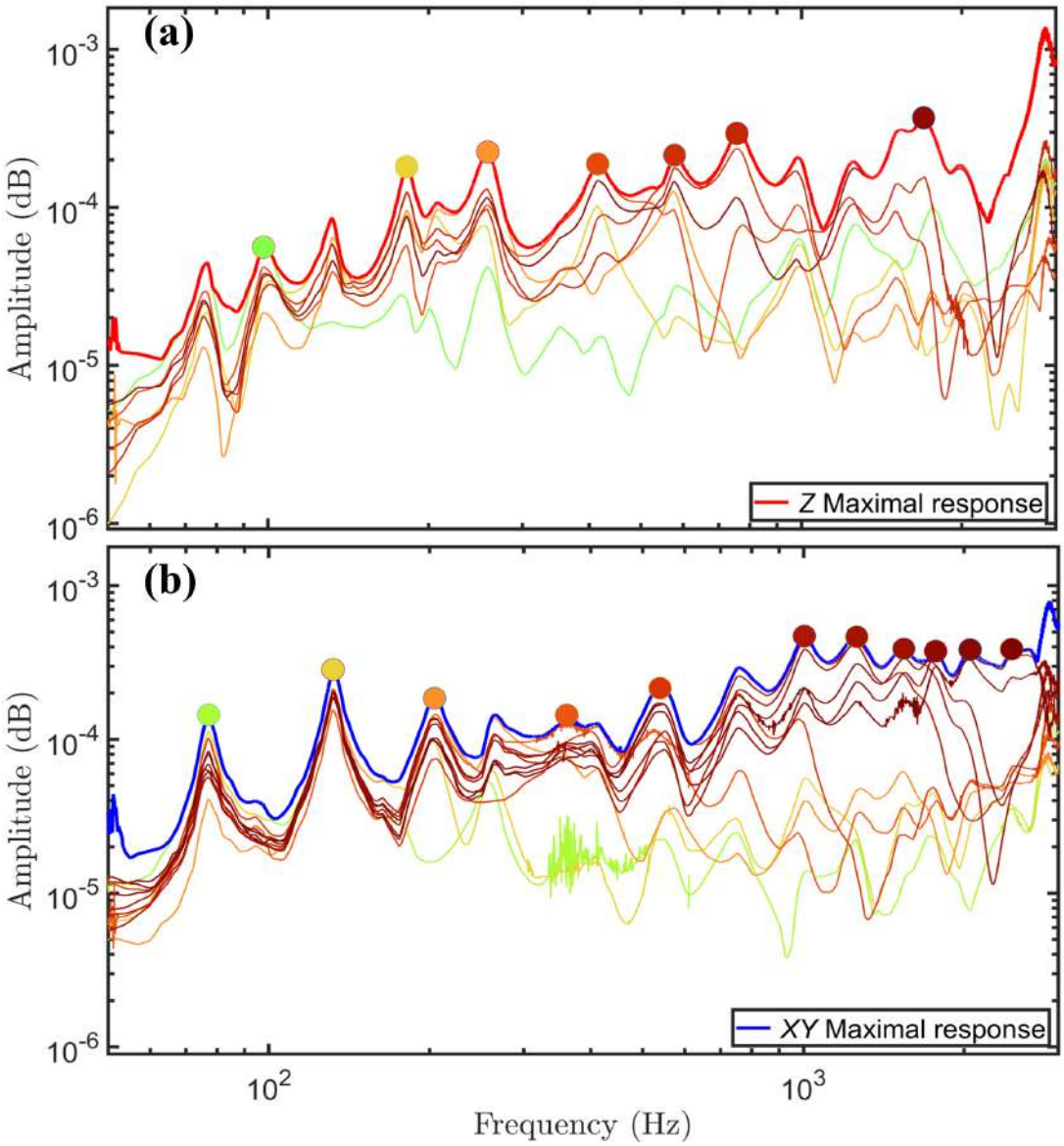

Figure 4. (a) Representative spectra of the *z* component of the particle velocity recorded at different locations. The colour of the curves corresponds to the location reported in figure 2. Symbols represent *Z* modes. The thick red line indicates the maximum velocity at each frequency. (b) The same as in (a) but for the *xy* component. The thick blue line indicates the maximum velocity at each frequency. Symbols represent *XY* modes.

obtaining two kinds of spectra, *xy* and *z*. Some spectra for the two cases are reported in figure 4a,b, respectively. For this measurement, the excitation signal was applied in the 45° direction. The colour of each spectrum corresponds to the curvilinear coordinate at which it has been measured, as indicated by the colour scale shown in figure 2. For a given eigenfrequency, indicated by a resonance peak in the spectrum, the amplitudes of the velocity components can change, depending on the location.

In general, for each frequency, there is a location in which the velocity amplitude is maximum at that frequency. By selecting, among all the spectra, the maximum amplitude for each frequency, we can obtain an 'envelope' of all the spectra, represented as a thick red line for the *z* component and as a thick blue line for the *xy* component in figure 4a,b, respectively. Since some resonance peaks can be detected both in the *xy* and in the *z* direction, by comparing the amplitude of those eigenmodes visible along both directions, we can assign a predominant vibrational character, *xy* or *z*, for each mode, depending on which vibration amplitude is larger. Peaks with a coloured symbol in figure 4a,b indicate eigenmodes that have a dominant *z* or *xy* vibrational character, respectively. The colour of the symbols represents the curvilinear coordinate at which their amplitude is maximum, following the colour scale of figure 2. It is possible to notice that the curvilinear coordinate of the peaks is increasing with increasing frequency, as expected in the case of a tonotopic behaviour.

3. Results

3.1. Tonotopic behaviour

For each mode, either XY or Z, the modal shape can be obtained by measuring, at the mode frequency, the velocity at each position along the curvilinear coordinate. Figure 5a,b reports the mode shapes obtained for several XY and Z modes, respectively, measured in the case of 45° excitation direction. Coloured symbols represent the magnitude of the velocity, according to the colour bar at the bottom of the figure. The red arrows indicate both amplitude and direction of the velocity, while the red star and blue arrow show the position and magnified velocity vector of the maximum particle velocity for that frequency. The tonotopic behaviour can be clearly observed for both XY and Z modes. Indeed, the position of the maximum (red star) moves at increasing curvilinear angles with increasing excitation frequency, showing the characteristic tonotopic spatial frequency mapping. These experimental modal shapes are compared, in appendix A, with their numerical counterparts obtained by finite-element analysis with COMSOL Multiphysics.

Full symbols shown in figure 3 report the experimental resonance frequencies as a function of the normalized curvilinear coordinate of the maximum particle velocity at that frequency. Results are reported for the three different excitation directions, 0°, 45° and 90°, in panels (a), (b) and (c), respectively. The insets show the transducers used for the three injection directions. Empty circles correspond to the relevant simulated eigenmodes, while the red and blue solid lines are an exponential fit of these eigenfrequencies, used as a guide to the eye to better highlight the simulated tonotopic behaviour. Figure 3a shows that, for the 0° direction, all the experimentally detected modes have a predominant XY character that indeed corresponds to the main direction of excitation. Along this direction, the transducer is not able to induce a predominant Z character in any of the modes detected. The situation changes when the device is excited along 45°, as shown in panel (b). Now we can observe both XY and Z modes, especially at low frequencies, while at higher frequencies the XY character is again prevailing, with the exception of a Z mode above 1500 Hz, which can also be seen in figure 4a. Moreover, when the device is excited along 90°, we observe a greater density of Z modes, which mainly vibrate along the excitation direction. The transducers have been attached by using cyanoacrylate glue, and a non-perfectly homogeneous connection could, in principle, play a role in the non-completely symmetrical behaviour. The error bars have been calculated by taking into account the fact that both measurements and simulations have been performed on a limited number of positions, namely 300 points for the simulations and 162 for the experiment, thus introducing an uncertainty in the position of the maximum response. This is more evident in the experimental data at high frequency, where, given the higher vicinity of the probed locations, a higher relative error on the determination of the curvilinear coordinate is introduced. Additional uncertainties stemmed from potential minor deformations of the sample over time and material property inconsistencies resulting from the 3D printing process. However, in all cases, a clear tonotopic effect has been observed, in agreement with the simulations. The behaviour is dependent on the direction of excitation, with a more comparable number of XY and Z modes around 45°. This result experimentally proves that the tonotopic effect can be realized simultaneously along two perpendicular directions of vibration.

3.2. Polarization behaviour

Figure 3 demonstrates that there is a correspondence between the maximum velocity response at a given frequency and the location where this occurs. We can call these locations 'tonotopic locations', i.e. the places where a certain frequency shows the maximum vibration. The device fabricated and experimentally tested here has been designed in order to approximately display the same tonotopic location for both families of modes, namely XY and Z. For each frequency, we can thus compare the xy and z components at the corresponding tonotopic location. Their relative magnitude is, in general, different and dependent on the excitation direction. Figure 6 shows, in a limited range of frequencies for clarity, the maximum of the two velocity components as a function of frequency, reported for the three excitation directions, 0°, 45°and 90° in panels (a), (b) and (c), respectively. As discussed above, here each frequency corresponds to a different location along the spiral. As expected, the xy component is dominating for a 0° excitation, and the opposite occurs at 90°, as already commented before when discussing the tonotopic behaviour. Finally, in the 45°case, the two components are more comparable in magnitude. In principle, the analysis of this kind of tonotopic spectra can provide information on the directionality of the input signal, once the metasensor has been fully characterized; that is, the spectra such as those shown in figure 6 have been ideally determined for all excitation directions. A convenient way to compare the two components can be to calculate the arctangent of their ratio. Since their behaviour depends on the excitation direction, this definition quantifies the output response in angular terms as well. We can thus define the output polarization as $\varphi^{out} = \arctan\left(\frac{U_{\parallel}^{out}}{U_{\perp}^{out}}\right)$, where $U_{\perp}^{out}$ and $U_{\parallel}^{out}$ are the xy and z components, respectively. Figure 7a reports the output polarization as a function of input frequency in the 60–200 Hz range, for the case of 45° excitation direction. The output polarization is significantly varying in the examined frequency range, i.e. from a minimum of approximately 0° at 65 Hz to approximately 80° around 180 Hz. φ^{out} is varying continuously with frequency: panels (b–k) report several examples of output polarizations corresponding to the coloured symbols shown in panel (a). The symbols are placed at the locations of the corresponding frequency, and the polarization value is represented by the angle that the coloured arrow forms with the horizontal axis. These polarization features allow us to potentially accomplish several tasks. One could determine the velocity field by measuring only one velocity component with a single LDV. Another functionality might be to obtain a desired output polarization over a wide range just by tuning the input frequency, thus selectively activating a dominant in-plane or out-of-plane vibrational behaviour, or a combination of the two.

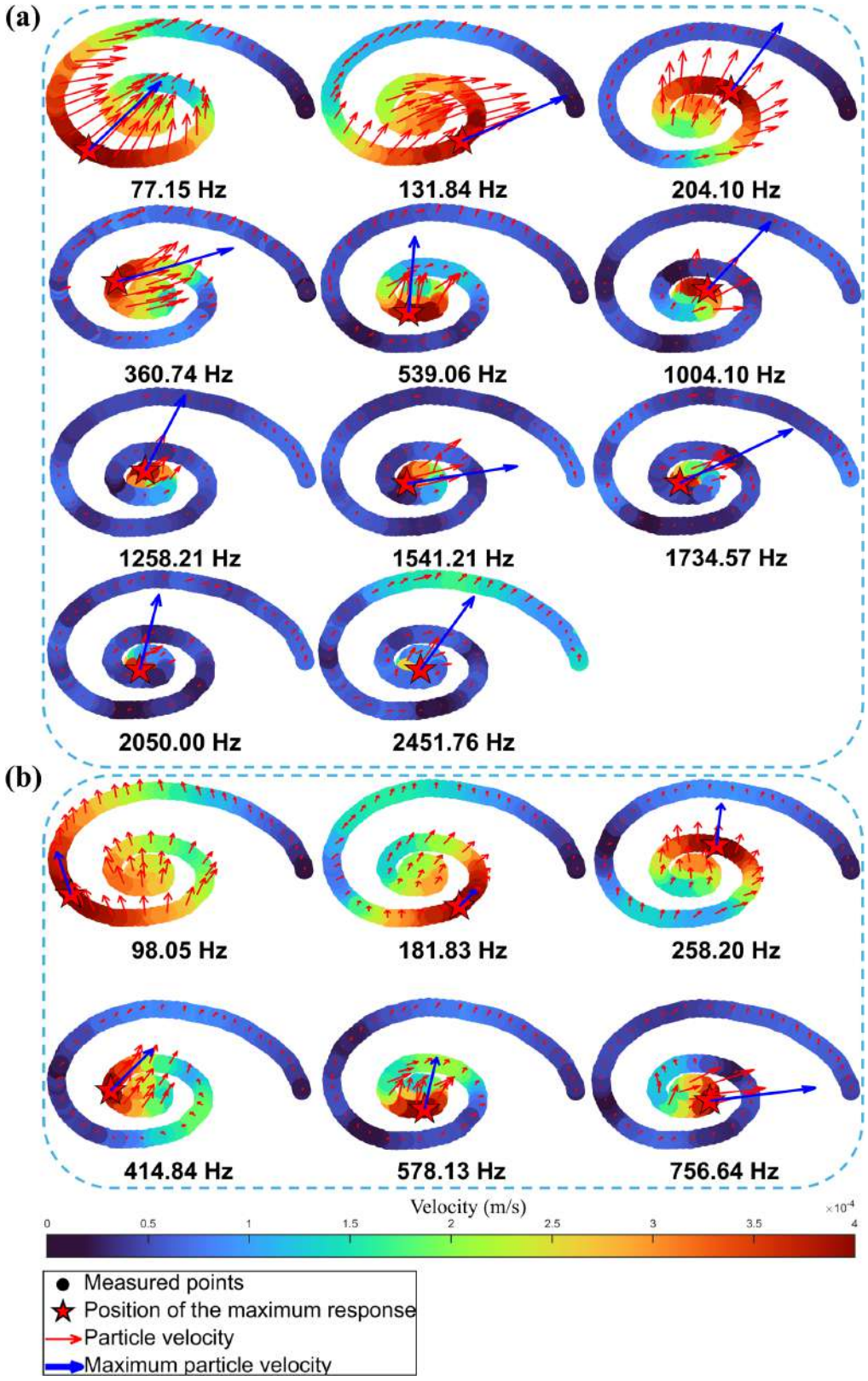

Figure 5. (a) Mode shapes that predominantly vibrate in the *xy* plane, called *XY* modes, in the case of 45° excitation. The red star shows the location of the maximum velocity, which falls at increasing curvilinear coordinates with increasing excitation frequency, as expected for a tonotopic behaviour. (b) Same as in (a) but for mode shapes that predominantly vibrate along the *z* direction, *Z* modes. The colourbar indicates the magnitude of the particle velocity at each location. Red arrows indicate the particle velocities at each point, while the blue arrow indicates the maximum particle velocity, which has been magnified for clarity.

4. Discussion

The metasensor described in this study, integrating bioinspired spiral geometry with both tonotopic and polarization-sensitive characteristics, has been demonstrated to be a versatile and powerful sensing tool, particularly suited for applications in structural health monitoring and non-destructive testing (NDT). Specifically, experimental results highlight two key functionalities that can be exploited. First, the sensor exhibits clear elastic tonotopic behaviour for the two components (in-plane and out-of-plane),

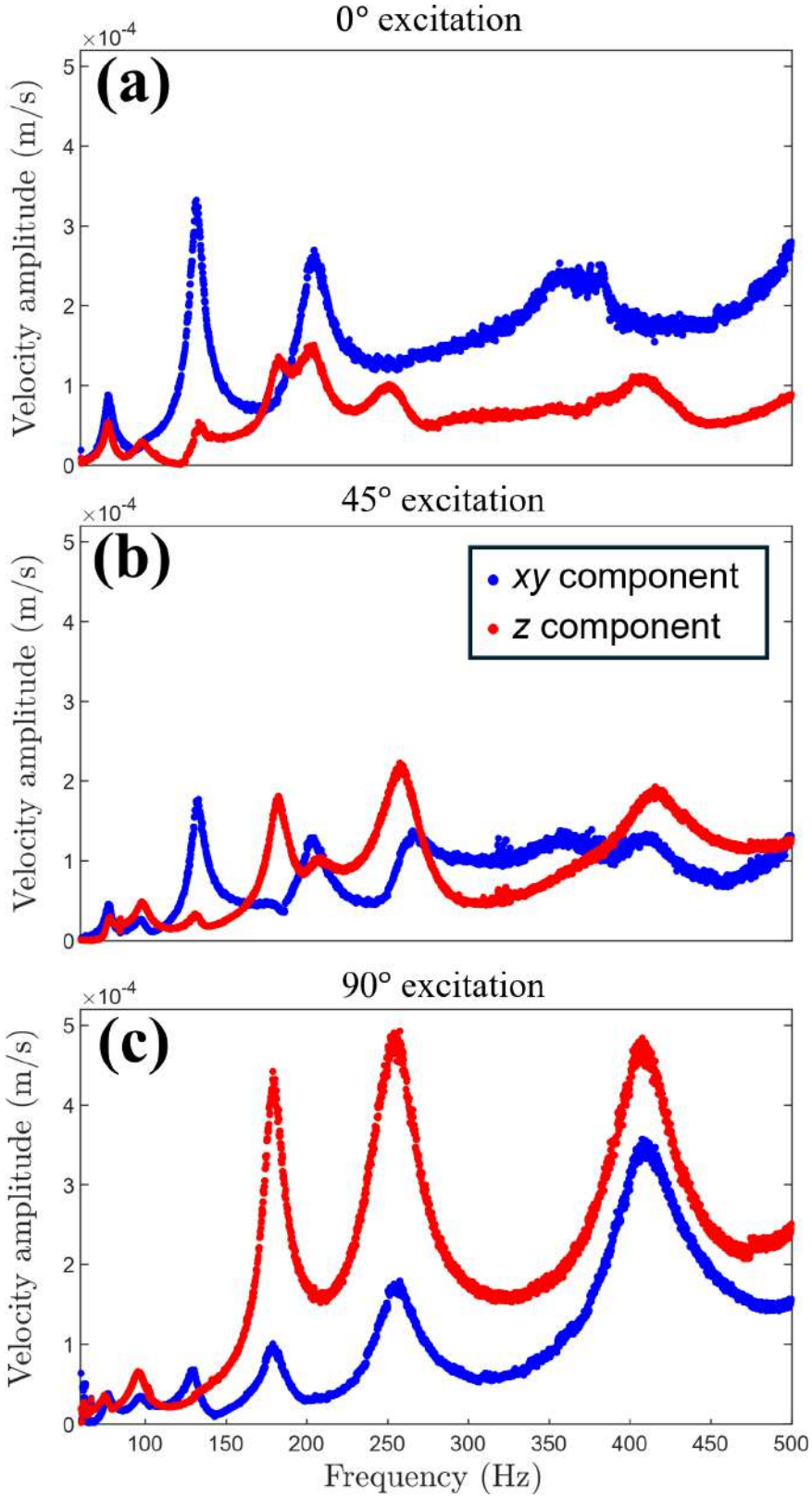

Figure 6. Experimental *xy* (blue) and *z* (red) components of the particle velocities along different excitation directions: (a) 0° excitation direction, (b) 45° excitation direction and (c) 90° excitation direction. The components are reported as a function of frequency in the 60–500 Hz range, and, for each frequency, the components have been measured in the location of their maximum value.

spatially mapping different frequency components of elastic vibrations along its spiral geometry. This capability of frequency separation can be exploited in nonlinear ultrasonic measurements, where structural defects such as cracks and delaminations typically generate nonlinear elastic responses, including higher harmonics. Traditional NDT methods rely heavily on detecting such nonlinear signatures to identify and characterize defects; however, spectral separation of the frequency components is often challenging. By exploiting the intrinsic elastic tonotopic design of the metasensor, the detection and separation of these nonlinear frequency components become significantly simpler, and this potentially increases the sensitivity to the nonlinear signature for the detection and characterization of the defect.

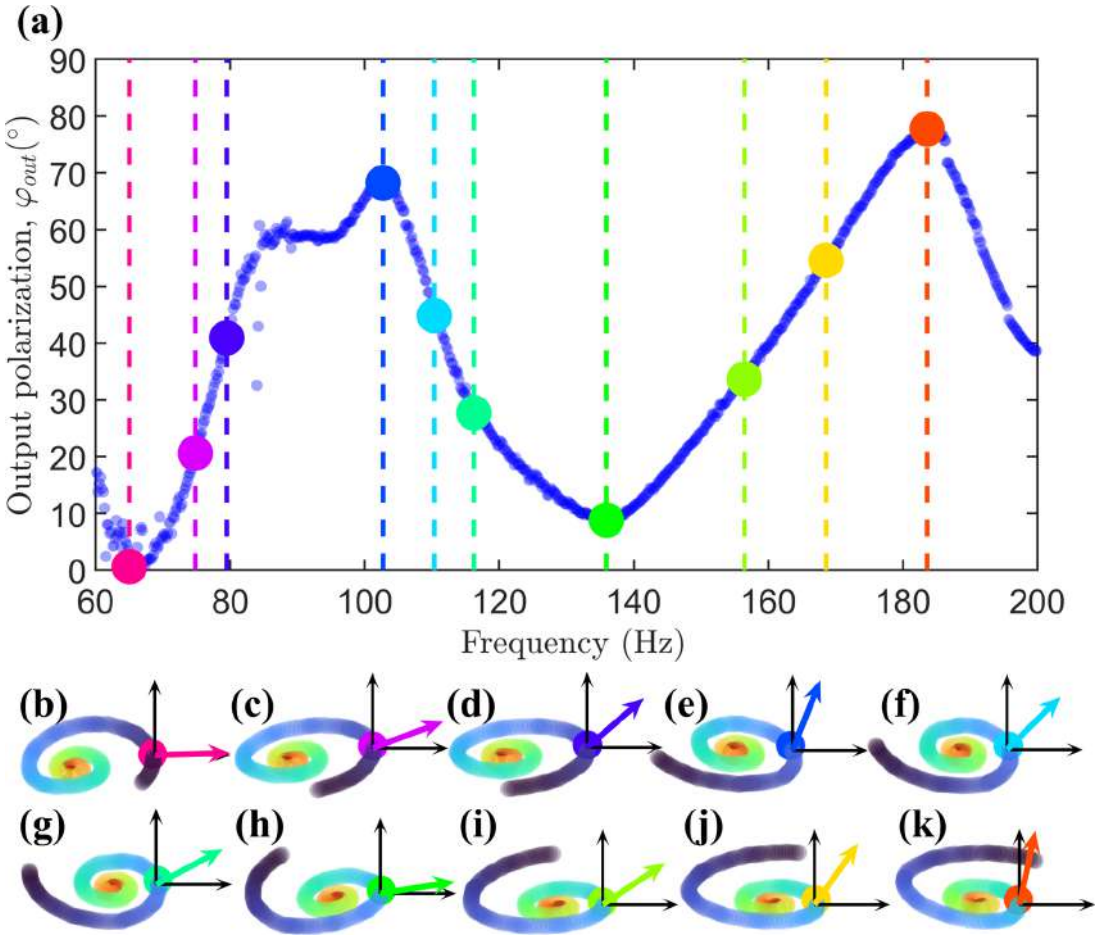

Figure 7. (a) Output polarization, $\varphi_{out} = \arctan\left(\frac{v_{\parallel}^{out}}{v_{\perp}^{out}}\right)$ as a function of frequency for the 45° excitation direction. At each frequency, the polarization is calculated at the location of the maximum velocity for that frequency. (b–k) The locations of the reported polarization are indicated by the coloured symbols, while the polarization value is represented by the angle formed by the coloured arrow with the horizontal axis. The colours of the symbols correspond to those reported in panel (a).

Secondly, the device demonstrates the polarization sensitivity in elastic vibrations, quantified experimentally through the output polarization angle, φ_{out}, defined as the arctangent of the ratio between the velocity components out of the plane (z) and in the plane (xy) (figure 7). This polarization sensitivity directly translates into the ability to determine the direction of propagation of incoming elastic signals. In practice, this allows for the localization of defect sources, even in situations where direct scanning (such as ultrasonic C-scans) is difficult or impossible due to limited physical access or complex geometries. By performing an initial calibration, i.e. mapping φ_{out} values to known directions of elastic excitation, the metasensor can subsequently identify the origin of unknown elastic signals, thus providing information about defect locations.

It is also possible to design structures with a cross-section that deviates from the simplest circular case, as is the case for real seashells like, for example, the *Otala lactea* or the *Pomacea diffusa* [11]. This allows us to add additional degrees of freedom in the design of the vibrational behaviour of the devices and engineer the tonotopic behaviour along the two different directions. The simplest shape after the circle is the ellipse. In this case, the cross-section radius is no longer constant at fixed curvilinear angle θ, and it can be written as $r(\theta,\varphi) = r_g(\varphi)\exp\left(k_b\frac{\theta}{\theta_{\max}}\right)$ [11]. $r_g(\varphi) = \frac{ab}{[(a\sin\varphi)^2+(b\cos\varphi)^2]^{1/2}}$, where $0 \le \varphi \le 2\pi$ is the angle between the semi-major axis of the ellipse a and the position vector of the cross-section point r_g while b is the semi-minor axis. The more the a/b ratio differs from 1, the more the moments of inertia corresponding to their direction will differ from each other. We could thus expect that, in these cases, the natural frequencies of vibration along the two directions will change with respect to the circular cross-section configuration. Figure 8a shows the case in which $a/b = 5$. It is possible to notice that the tonotopic behaviour for the two kinds of modes is still present, but now the two branches are separated, i.e. with respect to the tonotopic behaviour observed for the circular cross-section and reported in figure 1f, the natural frequencies of vibration for the Z modes are now lower than those for the XY modes, thus creating a different tonotopic behaviour along the two perpendicular directions. This is reasonable because the moment of inertia along a is larger than that along b and the natural frequencies of vibration around a certain axis are inversely proportional to the moment of inertia referred to that axis. Therefore, as shown in figure 8b, the two branches can also be separated in the opposite way, i.e. the Z modes will be above the XY ones, if the a/b ratio becomes less than 1, $a/b = 1/5$ in this case. Then, one can think of a structure in which the ratio between the two semi-axes varies continuously along the curvilinear angle. Figure 8c reports the case in which $a/b = 3$ at $\theta = 0$ and decreases continuously with increasing θ down to $a/b = 1/3$ at $\theta = \theta_{max} = 2\pi$. The two tonotopic branches are now crossing each other approximately halfway along the curvilinear path. Finally, it is also possible to reproduce the tonotopic trend typical of the real mammalian cochlea, in which the outer part of the spiral is more responsive to high frequencies while the inner part is more responsive to low frequencies [24]. This can be

achieved by continuously decreasing the stiffness with increasing curvilinear coordinate. The stiffness can be controlled indirectly through the curvature. The cross-section can thus be modified as $G(\varphi) \cdot r_g(\varphi)$, where $G(\varphi) = \alpha \cos(\varphi)$. Figure 8d reports the case for $\alpha = 0.5$, which corresponds to a stiffer outer region and a softer inner region. It is possible to see that in this case, we can obtain two inverted crossing tonotopic profiles. Although this geometry might be more difficult to fabricate compared with the previous ones, we can see another case in which, by keeping the material parameters constant and just by tuning some geometric features, we can obtain an additional, considerably different, elastic behaviour. The few examples reported here demonstrate that, not only in this kind of structure can the tonotopic behaviour be realized along two perpendicular directions, along xy and z, but, by suitably tuning the shape of the cross-section, the tonotopic branches can be decoupled and basically made independent from each other. The variation of the length of the two semi-axes of the ellipse is an example of how the moment of inertia about the two vibration directions can be tuned and, correspondingly, their natural frequencies varied. On the other hand, we have shown that the stiffness can be tuned indirectly by locally modifying the curvature.

Further engineering of the metasensor design could also be envisaged, like adding reinforcement masses in certain places or using the gradient of material properties, and so on. A particularly interesting scenario in this regard would involve designing a metasensor with opposite elastic tonotopic gradients along perpendicular vibration directions, an inverse tonotopy (high frequencies near the sensor's centre, low frequencies towards the extremity) along the xy-plane and a direct tonotopy (low frequencies near the centre, high frequencies towards the extremity) along the z axis. This dual tonotopic design could enable simultaneous yet independent detection and discrimination between surface and internal defects. Surface defects typically emit higher frequency signals and preferentially excite in-plane (xy) vibrations associated with symmetric Lamb wave modes, whereas internal defects, generating lower frequency signals, preferentially excite out-of-plane (z) vibrations associated with antisymmetric Lamb wave modes [35]. Thus, such an engineered configuration would enable the identification of defect type and location, simplifying and accelerating structural assessments in critical applications such as aerospace, civil engineering and advanced manufacturing.

5. Conclusions

Spiral structures, common to seashells and the cochlea, and in general widely recurring in nature, suggest interesting possibilities for the design of elastic metasensors with rich spectral features, i.e. tonotopy and polarization discrimination capabilities, which are reminiscent of well-known rainbow-trapping structures. We have fabricated one such device and experimentally validated its tonotopic response using a three-dimensional LDV. The seashell-inspired metastructure exhibits tonotopy for vibrations both within its plane and perpendicular to it. By selecting the excitation direction, these structures can preferentially activate in-plane or out-of-plane modes. We also demonstrate that the output polarization is tunable, i.e. by sweeping the input frequency, it allows for a transition from an almost purely in-plane vibration to a strongly dominant out-of-plane response. Moreover, by suitably tailoring the geometry, distinct tonotopic characteristics can be engineered independently along the two axes. Although the present design is passive, its architecture offers high design flexibility, allowing adaptation to different target frequency ranges through geometric scaling, material selection and reconfiguration of key parameters such as grading and coiling. These findings could be exploited to develop smart passive metasensors capable of intrinsic discrimination of frequency and polarization, with promising applications in structural health monitoring and NDT, where low-latency and low-power devices are of utmost importance.

Ethics. This work did not require ethical approval from a human subject or animal welfare committee.

Data accessibility. Experimental datasets supporting this article are provided as electronic supplementary material.

Supplementary material is available online [36].

Declaration of AI use. We have not used AI-assisted technologies in creating this article.

Authors' contributions. Y.L.: data curation, formal analysis, investigation, methodology, writing—review and editing; H.Z.: data curation, formal analysis, investigation, methodology, writing—review and editing; E.R.: data curation, investigation, methodology, writing—review and editing; N.M.P.: writing—review and editing; A.S.G.: conceptualization, methodology, supervision, writing—original draft, writing—review and editing; F.B.: conceptualization, funding acquisition, methodology, supervision, writing—original draft, writing—review and editing; M.T.: conceptualization, data curation, formal analysis, investigation, methodology, project administration, supervision, validation, visualization, writing—original draft, writing—review and editing.

All authors gave final approval for publication and agreed to be held accountable for the work performed therein.

Conflict of interest declaration. We declare we have no competing interests.

Funding. N.M.P., F.B. and M.T. are supported by the 'AMPHYBIA' project (2022ATZCJN)—funded by the European Union—Next Generation EU within the PRIN 2022 program (D.D. 104-02/02/2022 Ministero dell'Università e della Ricerca). N.M.P., A.S.G., F.B. and M.T. are supported by the European Union Horizon 2020 FET Open (Boheme) project under grant agreement no. 863179.

Acknowledgements. We thank G. De Sero for the 3D printing of the devices.

Appendix A. Modal shapes

Figure 9 reports a comparison between experimental and simulated modal shapes for the case of 45° excitation direction and of clamped-free boundary conditions. This is very important to unambiguously check that there is a correct match between experiments and simulations and to suitably compare the obtained tonotopic trends. Panel (a) shows some examples for the XY modes. The two left modes are experimental, the colour scale is proportional to the magnitude of the velocity and the red arrows indicate the magnitude and direction of the velocity. The two modes on the right in panel (a) are the corresponding simulated modes. Panel (b) shows analogous examples for two Z modes. In both cases, it is possible to see that there is a very good agreement between experiments and simulations, thus confirming what has been reported previously in figure 3.

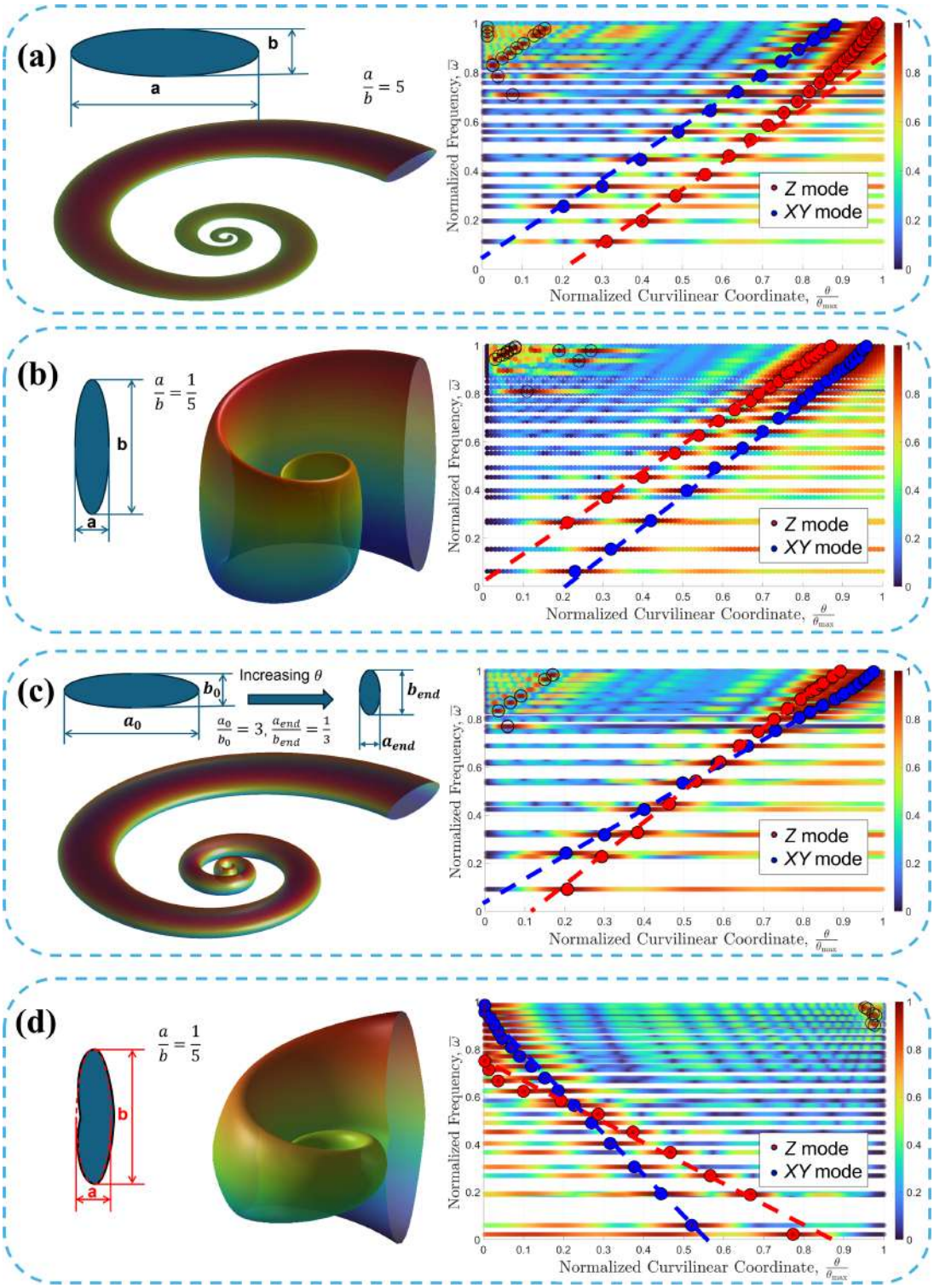

Figure 8. (a) By taking $a/b = 5$, where a is the in-plane and b is the out-of-plane semi-axis of the ellipse, it is possible to separate the two tonotopic branches. (b) If $a/b = 1/5$, the branches are separated in the opposite way. (c) By changing the a/b ratio from 3 to 1/3 along the curvilinear coordinate, the two tonotopic branches have different slopes and cross each other approximately halfway. (d) The stiffness can be varied by locally controlling the curvature, leading to an inverted tonotopic profile.

Appendix B. Free–free boundary conditions

In all the cases reported above in the paper, the boundary conditions were clamped-free. This is certainly a situation that more closely resembles the real mammalian cochlea, on one hand, and the possible real operating conditions of the devices, on the other hand. However, free–free boundary conditions were explored as well, as shown in figure 10. The figure reports the case of 45° excitation direction. The sensor has been suspended to reproduce as much as possible the free–free boundary conditions, as can be seen in the inset to the figure. The experiments have been compared with the simulations obtained with the same boundary conditions. Although it seems to deviate at high frequencies slightly more than in the case of the clamped-free configuration, in this case too the agreement is good, and we proved that the tonotopy can be achieved also for the free–free boundaries, both in

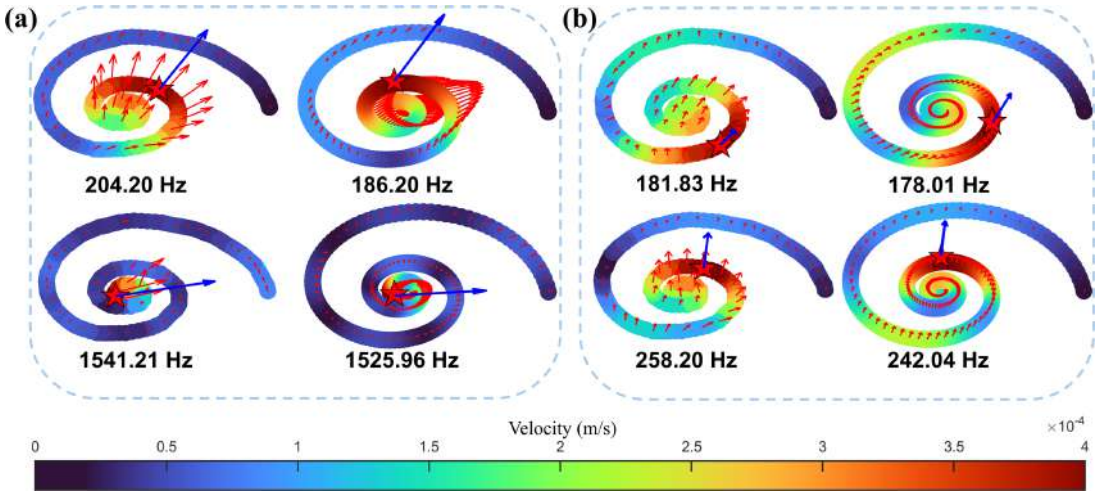

Figure 9. (a) Comparison between experimental (left) and simulated (right) modal shapes for two different *XY* eigenmodes under 45° excitation direction in case of clamped-free boundary conditions. (b) The same as in (a) but for the *Z* modes.

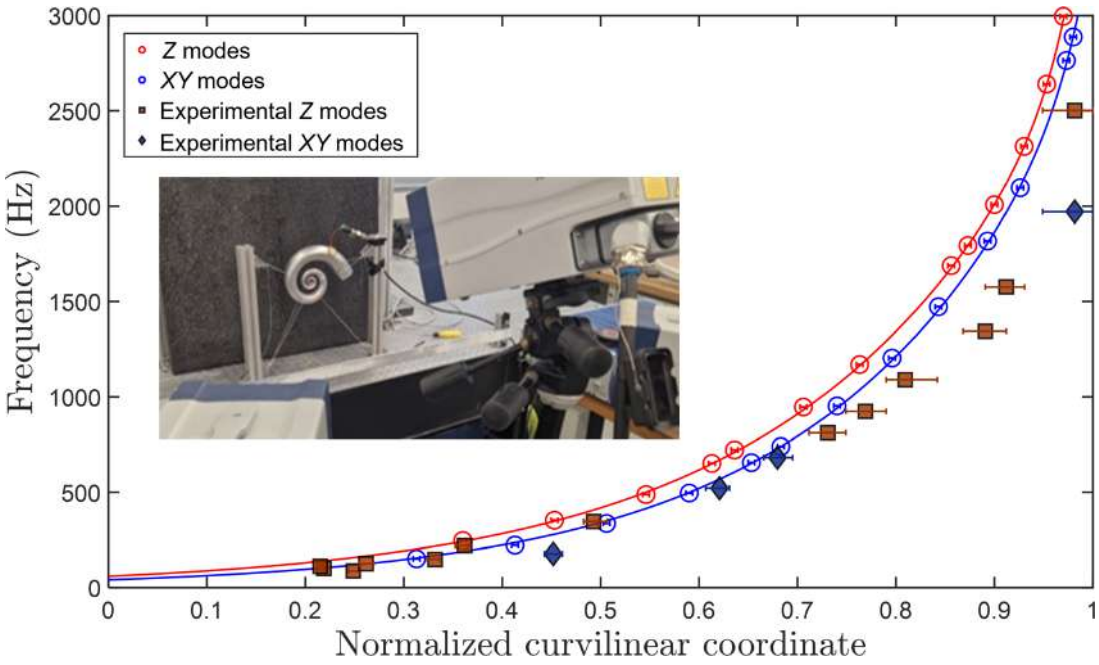

Figure 10. Tonotopic behaviour of the device under 45° excitation direction in case of free–free boundary conditions. Blue and red solid lines represent the tonotopic reference obtained by finite-element simulation, while the circular symbols indicate the frequency versus maximal response location of the simulated eigenmodes. Diamonds and squares represent the frequency versus normalized curvilinear angle for the experimental *XY* and *Z* modes, respectively. Error bars are obtained by taking into account the fact that the displacements are calculated or measured on a limited number of locations.

the plane of the spiral and perpendicular to it. It is worth noticing, however, that these conditions do not allow achieving the polarization capabilities reported for the clamped-free case.

References

1. Bosia F *et al*. 2022 Optimized structures for vibration attenuation and sound control in nature: a review. *Matter* **5**, 3311–3340. (doi:10.1016/j.matt.2022.07.023)
2. Fay RR, Dallos P. 2012 *The cochlea*. New York, NY: Springer Science, Business Media.
3. Robles L, Ruggero MA. 2001 Mechanics of the mammalian cochlea. *Physiol. Rev.* **81**, 1305–1352. (doi:10.1152/physrev.2001.81.3.1305)
4. Lighthill SJ. 2024 Biomechanics of hearing sensitivity. *J. Vib. Acoust.* **113**, 1–13. (doi:10.1115/1.2930149)
5. Manoussaki D, Dimitriadis EK, Chadwick RS. 2006 Cochlea's graded curvature effect on low frequency waves. *Phys. Rev. Lett.* **96**, 088701. (doi:10.1103/PhysRevLett.96.088701)
6. Surlykke A, Yack JE, Spence AJ, Hasenfuss I. 2003 Hearing in hooktip moths (Drepanidae: Lepidoptera). *J. Exp. Biol.* **206**, 2653–2663. (doi:10.1242/jeb.00469)
7. Schneider ES, Römer H, Robillard T, Schmidt AKD. 2017 Hearing with exceptionally thin tympana: ear morphology and tympanal membrane vibrations in eneopterine crickets. *Sci. Rep.* **7**, 15266. (doi:10.1038/s41598-017-15282-z)
8. Reid A, Marin-Cudraz T, Windmill JFC, Greenfield MD. 2016 Evolution of directional hearing in moths via conversion of bat detection devices to asymmetric pressure gradient receivers. *Proc. Natl Acad. Sci. USA* **113**, E7740–E7748. (doi:10.1073/pnas.1615691113)

9. Moulton DE, Lessinnes T, O'Keeffe S, Dorfmann L, Goriely A. 2016 The elastic secrets of the chameleon tongue. *Proc. R. Soc. A: Math., Phys. Eng. Sci.* **472**, 20160030. (doi:10.1098/rspa.2016.0030)
10. Porter MM, Adriaens D, Hatton RL, Meyers MA, McKittrick J. 2015 Why the seahorse tail is square. *Science* **349**, 1–7. (doi:10.1126/science.aaa6683)
11. Faghih Shojaei M, Mohammadi V, Rajabi H, Darvizeh A. 2012 Experimental analysis and numerical modeling of mollusk shells as a three dimensional integrated volume. *J. Mech. Behav. Biomed. Mater.* **16**, 38–54. (doi:10.1016/j.jmbbm.2012.08.006)
12. Johnson EH. 2021 Breaking down shell strength: inferences from experimental compression and future directions enabled by 3D printing. *Biol. Rev. Camb. Phil. Soc.* **96**, 1077–1091. (doi:10.1111/brv.12692)
13. Frenzel T, Kadic M, Wegener M. 2017 Three-dimensional mechanical metamaterials with a twist. *Science* **358**, 1072–1074. (doi:10.1126/science.aao4640)
14. Morvaridi M, Carta G, Brun M. 2018 Platonic crystal with low-frequency locally-resonant spiral structures: wave trapping, transmission amplification, shielding and edge waves. *J. Mech. Phys. Solids* **121**, 496–516. (doi:10.1016/j.jmps.2018.08.017)
15. Bae MH, Choi W, Ha JM, Kim M, Seung HM. 2022 Extremely low frequency wave localization via elastic foundation induced metamaterial with a spiral cavity. *Sci. Rep.* **12**, 3993. (doi:10.1038/s41598-022-08002-9)
16. Ciampa F, Mankar A, Marini A. 2017 Phononic crystal waveguide transducers for nonlinear elastic wave sensing. *Sci. Rep* **7**, 1–8. (doi:10.1038/s41598-017-14594-4)
17. Ghaffarivardavagh R, Nikolajczyk J, Glynn Holt R, Anderson S, Zhang X. 2018 Horn-like space-coiling metamaterials toward simultaneous phase and amplitude modulation. *Nat. Commun.* **9**, 1349. (doi:10.1038/s41467-018-03839-z)
18. Guo Y. 2025 Directional sound propagation in acoustic artificial structures. *Npj Acoust.* **1**, 8. (doi:10.1038/s44384-025-00009-6)
19. Yang C, Ren J. 2024 Chirality-induced phonon spin selectivity by elastic spin–orbit interaction. *Proc. Natl Acad. Sci. USA* **121**, e2411427121. (doi:10.1073/pnas.2411427121)
20. Ma F, Wu JH, Huang M, Fu G, Bai C. 2014 Cochlear bionic acoustic metamaterials. *Appl. Phys. Lett* **105**, 213702. (doi:10.1063/1.4902869)
21. Ma F, Wu JH, Huang M, Zhang S. 2016 Cochlear outer hair cell bio-inspired metamaterial with negative effective parameters. *Appl. Phys. A.* **122**, 1–8. (doi:10.1007/s00339-016-9668-8)
22. Zhao L, Zhou S. 2019 Compact acoustic rainbow trapping in a bioinspired spiral array of graded locally resonant metamaterials. *Sensors (Basel).* **19**, 788. (doi:10.3390/s19040788)
23. Rupin M, Lerosey G, de Rosny J, Lemoult F. 2019 Mimicking the cochlea with an active acoustic metamaterial. *New J. Phys.* **21**, 093012. (doi:10.1088/1367-2630/ab3d8f)
24. Dal Poggetto VF, Bosia F, Urban D, Beoletto PH, Torgersen J, Pugno NM, Gliozzi AS. 2023 Cochlea-inspired tonotopic resonators. *Mater. Des.* **227**, 111712. (doi:10.1016/j.matdes.2023.111712)
25. Chaplain G, De Ponti JM, Aguzzi G, Colombi A, Craster RV. 2020 Topological rainbow trapping for elastic energy harvesting in graded Su-Schrieffer-Heeger systems. *Phys. Rev. Appl.* **14**, 054035. (doi:10.1103/PhysRevApplied.14.054035)
26. De Ponti JM, Iorio L, Riva E, Ardito R, Braghin F, Corigliano A. 2021 Selective mode conversion and rainbow trapping via graded elastic waveguides. *Phys. Rev. Appl.* **16**, 034028. (doi:10.1103/PhysRevApplied.16.034028)
27. Nistri F *et al*. 2024 Efficient broadband sound absorption exploiting rainbow labyrinthine metamaterials. *J. Phys. D. Appl. Phys.* **57**, 245111. (doi:10.1088/1361-6463/ad3012)
28. Colombi A, Colquitt D, Roux P, Guenneau S, Craster RV. 2016 A seismic metamaterial: the resonant metawedge. *Sci. Rep.* **6**, 27717. (doi:10.1038/srep27717)
29. Liu Y *et al*. 2023 Multiscale static and dynamic mechanical study of the *Turritella terebra* and *Turritellinella tricarinata* seashells. *J. R. Soc. Interface* **20**, 20230321. (doi:10.1098/rsif.2023.0321)
30. Liu Y, Dal Poggetto VF, Gliozzi AS, Pugno NM, Bosia F, Tortello M. 2024 Seashell-inspired polarization-sensitive tonotopic metasensor. *APL Mater* **12**, 041104. (doi:10.1063/5.0201722)
31. Pappas JL, Miller DJ. 2013 A generalized approach to the modeling and analysis of 3D surface morphology in organisms. *PLoS One* **8**, e77551. (doi:10.1371/journal.pone.0077551)
32. Stratasys. 2020 *Material datasheet for Vero family 3D printing materials (PolyJet)*. See https://www.stratasys.com/siteassets/materials/materials-catalog/polyjet-materials/verovivid/mds_pj_vero_1020a.pdf.
33. Mora S, Pugno NM, Misseroni D. 2025 Programming the energy landscape of 3D-printed Kresling origami via crease geometry and viscosity. *Extreme Mech. Lett.* **77**, 102314. (doi:10.1016/j.eml.2025.102314)
34. Laude V. 2015 *Phononic crystals: artificial crystals for sonic, acoustic, and elastic waves*. vol. 26. Berlin, Germany: Walter de Gruyter GmbH & Co. KG.(De Gruyter studies in mathematical physics). (doi:10.1515/9783110302660)
35. Su Z, Ye L. 2009 *Identification of damage using Lamb waves*. vol. 48. London, UK: Springer.(Lecture notes in applied and computational mechanics). (doi:10.1007/978-1-84882-784-4)
36. Liu Y, Zhang H, Riva E, Pugno NM, Gliozzi AS, Bosia F *et al*. 2026 Supplementary material from: Experimental Demonstration of a Three-Dimensional Bioinspired Tonotopic Metasensor. Figshare. (doi:10.6084/m9.figshare.c.8230394)